Full Paper

Israel Journal of Chemistry

DOI: 10.1002/ijch.201500037

Solution X-ray Scattering Form-Factors with Arbitrary Electron Density Profiles and Polydispersity Distributions

Tal Ben-Nun,[a, b] Roi Asor,[a] Avi Ginsburg,[a, c] and Uri Raviv*[a]

Abstract: We present a method to calculate solution X-ray scattering form-factors of various geometries with generalized electron density and polydispersity profiles. We create arbitrary and physically relevant electron density profiles using a set of smooth hyperbolic tangent functions. To numerically calculate arbitrary electron density profiles, we formulate an algorithm that adaptively transforms the functions to a series of uniform discrete steps. We solve the models both numerically and analytically for the case of multiple spherical shells and compare the results to show the consistency of the algorithm. Other geometries are solved numerically. Various form-factors are analysed and compared with earlier results. We then compare polydispersity probability density functions (uniform, normal, and Cauchy distributions) of concentric hollow cylinder thicknesses. The relationship of the shape of arbitrary electron density profiles to the features of the scattering form-factor is discussed.

Keywords: density functional calculations · generalized electron density · SAXS · self-assembly · solution X-ray scattering

1. Introduction

Most involved biomolecular complexes cannot be crystallized and therefore have to be investigated in solution. Nuclear magnetic resonance (NMR), cryogenic transmission electron microscopy (cryo-TEM), dynamic light scattering (DLS), atomic force microscopy (AFM) in solution, solution neutron scattering, and solution X-ray scattering are methods that can be used to study complex supramolecular self-assembled structures in solution. It is often helpful to combine more than one method. Solution X-ray scattering methods have become one of the important tools for investigating the structure and interactions between complex molecular systems. Supramolecular self-assembled structures are composed of various shapes and often multilayers of those shapes. Each layer may have different thickness and mean electron density contrast, with respect to the solvent. The scattering signal has contribution from the shape and structure of the scattering objects, called the form-factor. The second contribution comes from the organization of the scattering object in space and is called the structure-factor.

Recently, solution X-ray scattering data analysis was standardized to a point of consolidating many form-factors into one application.[1] The analysis performed in all solution X-ray scattering applications, however, was based on concentric or layered geometries with radial or vertical electron density profiles based on sets of either Gaussian or Heaviside step functions (forming uniform discrete models).[2] (Uniform) step functions represent the electron density profile of concentric or layered objects with nonphysical variations that are infinitely sharp (see Figure 1). Whereas models composed of step functions are sufficient for low resolution form-factor analysis, such models have limited accuracy at higher resolution measurements performed at wider scattering angles.

Until recently, this issue was addressed in most of the common form-factors by replacing the uniform models with Gaussian-based electron density profiles.[2d] Nevertheless, the Gaussian-based profiles had three drawbacks. First, the mathematical derivation resulted in more computationally complex model functions. Second, the Gaussian functions approach 0 as $r \rightarrow \infty$, and third, multiple Gaussian functions cannot be smoothly combined with uniform models to create profiles that are both smooth and contain regions with any constant value.

[a] T. Ben-Nun, R. Asor, A. Ginsburg, U. Raviv
The Institute of Chemistry
The Hebrew University of Jerusalem
Jerusalem 91904 (Israel)
e-mail: uri.raviv@mail.huji.ac.il

[b] T. Ben-Nun
Department of Computer Science
The Hebrew University of Jerusalem
Jerusalem 91904 (Israel)

[c] A. Ginsburg
The Institute for Drug Research
The Hebrew University of Jerusalem
Jerusalem 91904 (Israel)

Supporting information for this article is available on the WWW under http://dx.doi.org/10.1002/ijch.201500037.

Israel Journal of Chemistry

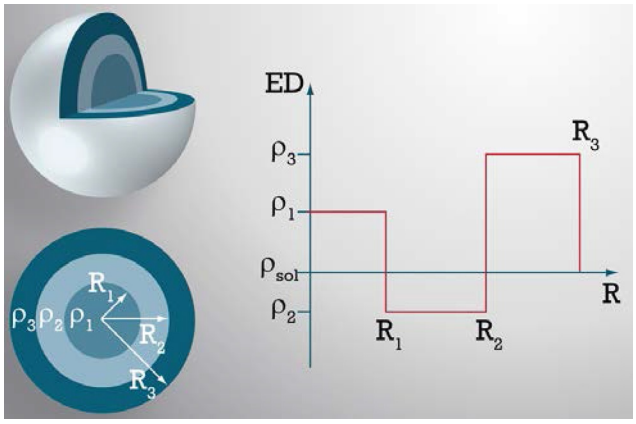

Figure 1. Illustration of the uniform spherical multilayered shell model. The top- and bottom-left portions of the figure show a sliced 3D representation and a 2D cross-section of the model, whereas the right-hand side plots the corresponding radial ED profile as a function of the radius R. R_i and ρ_i are the radius and electron density of the i^{th} layer, respectively.

In this paper, we present a generic approach for electron density profile modeling, which allows the computation of any arbitrary electron density profile function and the use of it as the basis for computing form-factors for fitting the signal. Hyperbolic tangent functions are smooth and may replace the step function used for the uniform models. Owing to the smoothing factor contributing an additional degree of freedom, these functions are expected to generate more accurate results than the step function, particularly above the scattering vector amplitude, q, values that correspond to real-space correlation distances that are of the order of the variations of the electron density profiles. After presenting the algorithm that allows the calculation of general electron density profiles, its correctness is shown to be maintained by deriving the spherical form-factor with the hyperbolic tangent functions semi-analytically and comparing the resulting signals.

Another application of the arbitrary profile algorithm is in polydispersity probability density functions. By generalizing the pattern in which the form-factors are polydispersed, we are able to obtain more physically relevant information about the underlying variations of self-assembled structures. The infrastructure for small-angle X-ray scattering (SAXS) model fitting in X+[1] allowed us to build and test the arbitrary profile algorithm, and arbitrary profiles are now one of the new features of the program.

The paper is organized as follows. Section 2 describes the underlying theory of electron density profiles, polydispersity distributions, and their relevance to SAXS. We then elaborate on the candidate replacement for the discrete step profile in Section 3. Section 4 describes and formulates the algorithm for profile discretization. Finally, various results of self-assembled biomolecules are presented and discussed in Section 5, and conclusions are made in Section 6.

2. Theory

2.1. Electron Density Profiles

Solution X-ray scattering theory specifies that for any object of volume, V, the scattering amplitude, $F(\vec{q})$, as a function of the momentum transfer vector, $\vec{q}$, is given by the Fourier Transform of its electron density contrast, $\Delta\rho(\vec{r})$, with respect to the solvent:[3]

$$F(\vec{q}) = \int_V \Delta\rho(\vec{r}) \exp(i\vec{q}\cdot\vec{r})d\vec{r}.$$

The electron density contrast originates in the different molecular composition of the scattering objects with respect to the surrounding solvent. The measured form-factor intensity is the square of the scattering amplitude: $|F(\vec{q})|^2$. In solutions (or powders), $|F(\vec{q})|^2$ should be averaged over all the possible orientations (OA):

$$I(q) = \left\langle |F(\vec{q})|^2 \right\rangle_{OA} = \int_0^{2\pi} d\phi_q \int_0^{\pi} d\theta_q |F(\vec{q})|^2 \sin\theta_q.$$

The reciprocal space vector, $\vec{q}$, is given by: $\vec{q} = (q, \theta_q, \phi_q)$ in spherical coordinates, and $\vec{r} = (r, \theta, \phi)$ is the position vector in real space.

Owing to the isotropic characteristic of complex fluid samples in solutions, the two-dimensional scattering pattern, measured on an area detector,[4] is radially symmetric. Because of this, the scattering pattern is radially integrated using Fit2D[5] and the relevant information is projected to a one-dimensional scattering signal of the scattering intensity as a function of q, the magnitude of $\vec{q}$. The 1D signal is then analyzed. In the case of a one-dimensional radial electron density profile function, $\rho(r)$, the profile represents the variation in the electron density from the center outwards, where $r = |\vec{r}|$.

The discrete step radial electron density profile function is as follows:

$$\rho(r) = \rho_0 + \sum_{i=1}^{N} \Delta\rho_i[\theta(r - R_{i-1}) - \theta(r - R_i)],$$

where $\Delta\rho_i$ is the electron density contrast between layer i and the solvent ρ_0, R_i is the thickness of layer i, and $\theta(r)$ is the Heaviside step function. We define the one-dimensional radial electron density contrast profile to be $\Delta\rho(r) = \rho(r) - \rho_0$. In the case of layered structures, a mathematically similar profile is used, but a selected direction (e.g., z) replaces the r dependence, and the R_i variables are replaced by layer thicknesses in that direction.[2d]

2.2. Form-Factor Polydispersity

In solution, self-assembled or supramolecular structures may be polydispersed, as they often do not have uniform size and shape. Polydispersity for the case of one size parameter is already computed for SAXS,[1] and uses the normal distribution function for any one size parameter. We wish to generalize both the single parameter and the probability density function of the polydispersed model in solution. Multiple parameter polydispersity of a subset $S_1,\ldots, S_k$ of n parameters is defined as follows:

$$\int_{-\infty}^{\infty} P_{S_1}(p'_{S_1}) \cdots \int_{-\infty}^{\infty} P_{S_k}(p'_{S_k}) I(q,\vec{p}') dp'_{S_1} \cdots dp'_{S_k},$$

where $\vec{p}'$ is a modified parameter vector consisting of $\vec{p}$ and the polydispersed parameters, and each parameter p'_{S_i} is dispersed with the probability density function, P_{S_i}.

The arbitrary profile algorithm was applied to the polydispersity engine of X+ to support both multiple parameters, according to the above equation, and arbitrary probability density functions. Three sample distributions were added to the program: uniform, normal and the Cauchy distributions. Any probability density function may be input to the algorithm, including multimodal distributions that can represent several subpopulations, as often is the case in out-of-equilibrium states.

3. Hyperbolic Tangent Profile

We would like to choose a smooth function $\phi(r)$ that generalizes the discrete step profile function to include varying slopes. The function should therefore satisfy the following set of equations:

1. $\lim_{r\to-\infty} \phi(r) = 1$
2. $\lim_{r\to-\infty} \phi(r) = 0$
3. $\lim_{\alpha\to\infty} \phi(\alpha r) = \theta(r)$

In the form $\phi(\alpha(r-R))$, the slope and position of the midpoint will be characterized by α and R respectively.

The Heaviside step function is replaced with the following hyperbolic tangent-based function:

$$\phi(r) = \frac{\tanh(r)+1}{2}.$$

The correctness of the hyperbolic tangent as a profile function is fully derived in Section 1 of the supporting information. Replacing θ with ϕ, we obtain, for the case of radial electron density profiles:

$$\rho(r) = \rho_0 + \sum_{i=1}^{N} \Delta\rho_i \{\phi[\alpha_{i-1}(r-R_{i-1})] - \phi[\alpha_i(r-R_i)]\},$$

where α_1 is the slope, or inverse smoothing factor, of the i^{th} layer. Note that when summing over several layers, the slopes may cause negative contribution (compared with the solvent electron density, ρ_0) to the overall electron density contrast profile, since the layer transitions are not immediate as in the models using the Heaviside step functions. Similar substitutions are used in other types of one-dimensional electron density profiles.

3.1. Analytic Hyperbolic Tangent Electron Density Profile of a Sphere

Using the replacement function $\phi(r)$ and the continuous $\rho(r)$ profile function from the last equation, we proceed to semi-analytically derive a hyperbolic tangent-based form-factor of multiple spherical shells. The scattering amplitude is given by:

$$F(\vec{q}) = \int_V \Delta\rho(|\vec{r}|) e^{i\vec{q}\cdot\vec{r}} d\vec{r}.$$

Using polar coordinates, in which $\vec{q} = (q, \theta_q, \phi_q)$, the sphere is modeled as follows:

$$F(\vec{q}) = \frac{4\pi}{q} \int_0^{\infty} \Delta\rho(r) r \sin(qr) dr.$$

The full derivation is provided in Section 2 of the supporting information.

Because we obtained an upper limit for each layer in the profile function, the above improper integral is calculated numerically from 0 to $\max_{1\le i\le N}[R_i + (10.36/\alpha_i)]$ (see Section 1 of the supporting information). Due to the symmetry of the spherical model on both polar axes, the resulting intensity is:

$$I(q) = \langle |F(\vec{q})|^2 \rangle_{OA} = |F(\vec{q})|^2.$$

4. Profile Discretization

Arbitrary electron density profiles and polydispersity distributions can be computed by performing discretization on the profile functions and transforming them to a sum of Heaviside step functions. Any continuous function, f, defined in the range $[a,b]$, is represented by a discrete set of N ordered pairs $(s_i, f(s_i))$ such that the set approaches the function as accurately as necessary. Accuracy increases with N, but does so in the cost of performance, due to the amount of points computed after discretization. We define f_d to be the desired discrete version of f, using the

Heaviside step function as the basis for the discrete steps, as follows:

$$f_d(x,N)=\sum_{i=1}^{N} f\left(\frac{s_{i-1}+s_i}{2}\right)[\theta(x-s_{i-1})-\theta(x-s_i)],$$

where $s_0=0$.

Our discretization process uses two different methods: static subdivision and dynamic (adaptive) subdivision. Static subdivision dictates that f_d comprises exactly N steps, whereas the adaptive subdivision discretization method specifies a desired ε such that, with a minimal number of discrete steps (N), it will satisfy:

$$\left|\int_a^b (f(x)-f_d(x,N))dx\right|<\varepsilon. \quad (1)$$

Both methods are proven in Sections 3 and 4 of the supporting information.

4.1. Dynamic Subdivision

Since the accuracy of the discretization depends not only on the number of steps, but also on df/dx (i.e., a function that changes rapidly will require more steps than a constant function, which requires only one step), we formulate an algorithm that, for every function, f, defined in the range $[a,b]$, there is a minimal nonuniform grid of steps created that best represents f by satisfying Eq. (1). The adaptive algorithm (Figure 2) performs a process reminiscent of adaptive quadrature algorithms.[6] The algorithm generates a single-step f_d (using the midpoint method)[7] for the input range, and compares its integral with a more accurate version of the integral of f using Simpson's rule, in that range. If the difference is smaller than ε, the algorithm converges on this single step as the best discrete step representative of f. Otherwise, the range is subdivided into two halves, and the algorithm is recursively computed on each of the two subranges with $\varepsilon/2$ as the target difference. Finally, the results are summed and the step sets are unified to obtain the final result. The algorithm in Figure 2 computes the integral by initializing *steps* as an empty set, and returns both *steps* and the result of the quadrature, accurate up to the input ε.

Note that due to performance considerations, the actual algorithm uses another parameter: maximal recursion depth (*depth*). With each recursion step, the parameter is passed as *depth*−1, and when *depth* reaches zero, no further recursion is performed. This modification also causes the amount of steps to be bounded by 2^{depth}, since a full binary tree of height *depth* will not contain more than 2^{depth} elements.

To eliminate redundant consecutive steps that have the same function value, the algorithm iterates over *steps* one final time to combine consecutive steps whose height difference is less than ε.

procedure *AdaptiveQuad*:
Inputs: $f, a, b, \varepsilon, steps$
Outputs: $value, steps$

1. Insert $\frac{a+b}{2}$ to *steps*
2. $midpoint \leftarrow (b-a) f\left(\frac{a+b}{2}\right)$
3. $simpson \leftarrow \frac{b-a}{6}\left[f(a)+4f\left(\frac{a+b}{2}\right)+f(b)\right]$
4. **if** $|midpoint-simpson|<\varepsilon$
5. **return** *simpson*
6. **else**
7. **return** $AdaptiveQuad\left(f, a, \frac{a+b}{2}, \frac{\varepsilon}{2}, steps\right) + AdaptiveQuad\left(f, \frac{a+b}{2}, b, \frac{\varepsilon}{2}, steps\right)$
8. **end if**
9. **end procedure**

Figure 2. Adaptive function discretization algorithm.

The error[7] of the midpoint method is $-\frac{1}{24}(b-a)^3 f^{(2)}(a)+O((b-a)^4)$, and the error[8] of Simpson's rule is $\frac{1}{90}\left(\frac{b-a}{2}\right)^5 |f^{(4)}(c)|$, where c is some number between a and b. Therefore, Simpson's rule will necessarily result in more accurate results than the single step.

5. Results and Discussion

To test the validity and accuracy of our algorithm, we verified a numerical Gaussian electron density profile against an analytical one that was previously derived.[2d] The same was performed for the hyperbolic tangent model and its analytic counterpart, shown in Section 3.1.

This section presents both the simulated and experimental results of arbitrary electron density profiles and polydispersity probability distribution functions. More results appear in Section 5 of the supporting information.

5.1. Electron Density Profiles

We compare different types of electron density profiles and show their effect on SAXS form-factors. Figure 3 compares the discrete step uniform electron density profile (solid blue curve) and hyperbolic tangent profiles with various slopes of a hollow sphere. The dimensions of the simulated hollow sphere are: inner radius of 8 nm and

Israel Journal of Chemistry

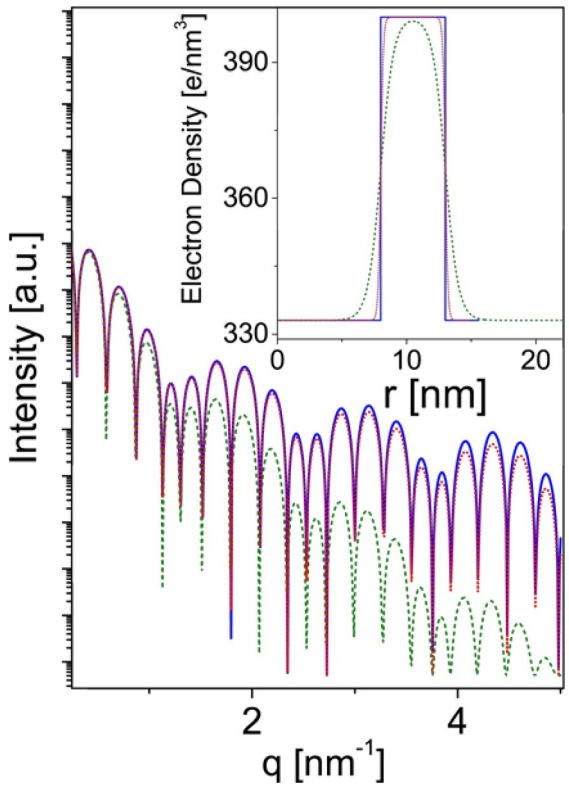

Figure 3. Comparison between the scattering intensity of the hollow spherical model with discrete electron density profile (blue curve) and the hyperbolic tangent profile with varying slopes (dotted red and dashed green curves). The inset shows the corresponding radial electron density profiles as a function of the radius, *r*.

outer radius of 13 nm, with an electron density contrast of 67 $e\,\mathrm{nm}^{-3}$ at the outer shell. The green dashed and red dotted curves represent the same model with a discretized hyperbolic tangent profile having slopes (α, as described in Section 3) of 1 and 5 respectively. Note that all three profiles are very close in small scattering angles (low q values) and diverge as the scattering angle becomes wider (high q values).

Despite the apparent faster decay of the amplitudes of the smoother profiles, the minima of the form-factor when the slopes of the electron density profile are equal (as in Figure 3) remain unchanged as the slopes decrease. This result suggests that the minima are predominantly set by the center-of-mass of the electron density contrast, rather than the tails of the profiles, and the amplitudes of the form-factor oscillations decay slower as α increases.

Figure 4 shows how the same result is achieved in a stack of two infinite flat slabs[2d] with different electron densities and thicknesses. The figure emphasizes the fact that, although the profiles are different in terms of layer transition slopes, the minima of the model are located at the same q offsets until the slope significantly decreases (see the case of $\alpha = 0.2$ or 1).

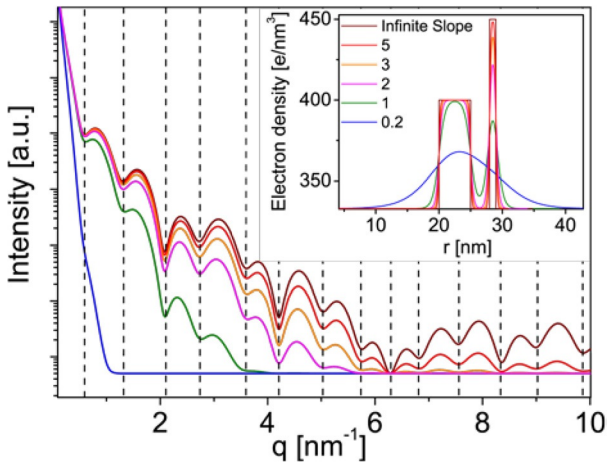

Figure 4. Comparison of various hyperbolic tangent slopes and their effect on a model of a stack of two infinite flat slabs at high *q*-range.

To verify that this phenomenon does not stem from the electron density per unit area $\left(\int \rho(r)dr\right)$, we tested the case of asymmetric slopes with a single layered spherical shell (inner radius of 4 nm, outer radius of 7 nm, with an electron density contrast of 67 $e\,\mathrm{nm}^{-3}$). The results are shown in Figure 5. In this case, the slopes have a visible effect on the locations of the intensity minima and the frequency of the oscillations, even though the electron density profile per unit area does not change. We speculate that the center of mass of the electron density profile, $\int r\rho(r)dr / \int \rho(r)dr$, which does not change in Figures 3 and 4, determines the form-factor minima and oscillation frequency.

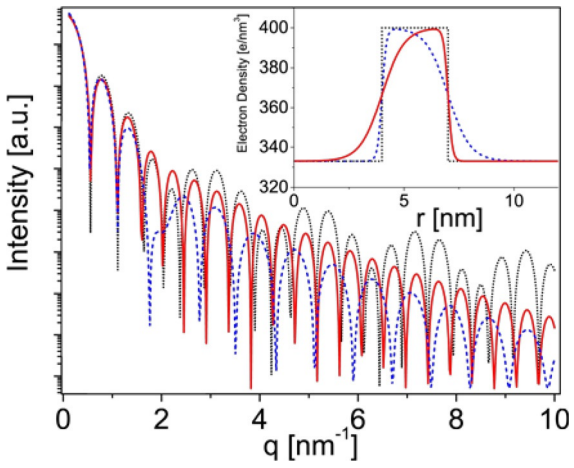

Figure 5. Comparison of asymmetric slopes in a spherical shell model. The dotted curve represents the uniform model, while the solid red and dashed blue curves represent the asymmetric hyperbolic tangent slope models. In the red curve, the slopes are $\alpha_1 = 1$ and $\alpha_2 = 5$, whereas in the blue curve, the slopes are $\alpha_1 = 5$ and $\alpha_2 = 1$.

5.2. Experimental Results

In our earlier paper,[2d] we examined the scattering of 1,2-dioctadecanoyl-sn-glycero-3-phospho-L-serine (DSPS) membranes. The same data is shown in Figure 6.

In the earlier paper all the experimental details were provided and two models were examined:

1. A stack of infinite flat uniform slabs with varying electron density.
2. A stack of infinite flat slabs having a Gaussian electron density profile along the normal direction.

Both models comprised 3 layers, one for each lipid headgroup located at the membrane/water interface and one for the central region of the hydrophobic lipid tails. The uniform model did not fit well to the data, particularly at higher q values. The Gaussian model was able to provide a good fit, however, a very sharp Gaussian function was assumed to represent the hydrophobic tail region. We then did not have the option to eliminate this sharp contribution within the Gaussian model and examine its physical relevance.

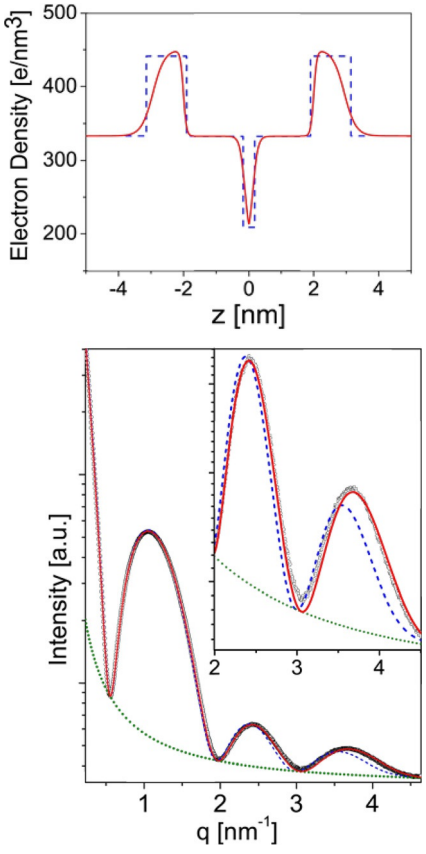

Figure 6. Fitting results of a radially integrated DSPS membrane scattering signal. The uniform and hyperbolic tangent models are highlighted in blue dashed and solid red curves, respectively. The assumed power-law background of the signal is shown as a broken dark green curve. The power-law used is: $25.8q^{-1.278}+25.71$.

Using the hyperbolic tangent model, we found a better fit to the data, but this required a third central sharp and narrow layer at the center. We then added an equivalent layer to the uniform model, which massively improved the quality of our fit. We attribute this lower electron density contrast at the center of the gel-phase of DSPS to the CH_3 groups in the end of the lipid tails that assume a larger volume than the rest of the CH_2 groups on the tails. Because the bilayer is in gel-phase, it forms a rather uniform sheet that has little flexibility and therefore cannot optimize its packing. By adding the lower density layer at the center of the tail region in the uniform model, an adequate fit was obtained. Using the smooth profile improved the fit to a certain degree. Without the central low density layer, even the smooth hyperbolic tangent models did not fit the data well, suggesting that the smooth models improve the fit at this q-range without significantly changing the characteristics of the electron density profile.

We also studied[9] the structure of the empty capsid of Simian Virus 40 (SV40), composed of three structural proteins: VP1; VP2; and VP3. VP1, the major capsid protein, forms the contiguous capsid of SV40. SV40 VP1 virus-like particles (VLPs) were expressed in *Spodoptera frugiperda* (Sf9) and purified by Stanislav Kler and Ariella Oppenheim, as described elsewhere.[10] The buffer solution was measured at the same capillary spot and subtracted from the empty capsid signal. Figure 7 uses spherical shell models and compares the uniform and smooth profiles. The smooth hyperbolic tangent profile can fit the data well without producing additional oscillations at high q values as the discrete model does; thus, the smooth model is more physically relevant.

6. Conclusion

The main advantage of the hyperbolic tangent smooth profiles is their physical relevance, as they better represent the state of many molecular self-assembled structures. Their ability to create smooth transitions from one electron-density layer to another cannot be achieved with any of the earlier models. Uniform models can still be used, but may yield additional oscillations that are not observed in experimental data at wide scattering angles.[2d] Gaussian profile functions are smooth, but inadequate for solution X-ray scattering analysis in some cases, because they decay to baseline, and therefore cannot remain at a constant electron density level (unless several functions are added). This drawback increases the number of degrees of freedom in the model and comes with a computational cost and weaker physical relevance. Empirically, we found that symmetric smooth profiles change the amplitude of the form-factor oscillations, how-

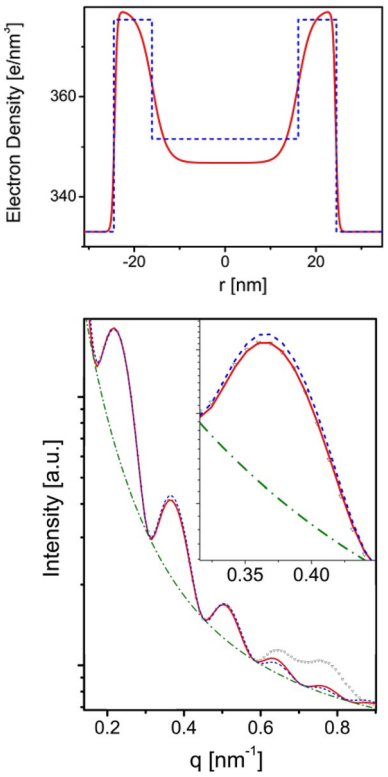

Figure 7. Radially integrated scattering signal of the empty capsid of the SV40 virus (black open symbols). The dashed blue curve corresponds to the best fit uniform spherical shell model. The solid red curve corresponds to the hyperbolic tangent model that best fits the data. The dark green dash-dotted curve is the assumed power-law background that goes through the minima of the signal. The inset zooms-in on the second lobe. The top graph presents the radial electron density profiles of the two models. The power-law used for the background function is: $0.566q^{-0.363} + 0.077q^{-2.836}$.

ever, as long as all the slopes are equal, the minima remain unchanged. When the slopes were significantly low, minima at wide scattering angles diminished. We attribute the preservation of the minima locations to the fact that the center of electron density mass did not change under those conditions.

As for polydispersity probability distribution functions, the chosen function depends on the type of polydispersity and the amount of expected localization of the mode (point of highest probability). For evenly polydispersed parameters, uniform distribution performs well. For uneven modal distributions, we found that the normal distribution results in slightly shifted oscillations and higher minima, whereas the Cauchy distribution maintains the offsets of the oscillations better. The minima in the Cauchy distribution, however, are lower than in the normal distribution. Finally, multimodal polydispersity profiles can better represent population mixtures.

Acknowledgements

We thank Daniel Harries for helpful discussions and Slava Kler, Orly Ben-Shaul, and Areilla Oppenheim for experimental help with the SV40 VLPs. The ESRF synchrotron, beamline ID02 and Elettra, 5.2L SAXS beamline are acknowledged, as the presented data were acquired there. This project was supported by the Israel Science Foundation (grant number 1372/13), the US-Israel Binational Science Foundation (grant number 2009271), Kamin program of the chief scientist of Israel Ministry of Economy, and the FTA-Hybrid Nanomaterials program of the Planning and Budgeting Committee of the Israel Council of Higher Education. We thank the Safra, Wolfson, and Rudin Foundations for supporting our laboratory.

References

[1] T. Ben-Nun, A. Ginsburg, P. Szekely, U. Raviv, *J. Appl. Crystallogr.* **2010**, *43*, 1522–1531.

[2] a) A. Steiner, P. Szekely, O. Szekely, T. Dvir, R. Asor, N. Yuval-Naeh, N. Keren, E. Kesselman, D. Danino, R. Resh, A. Ginsburg, V. Guralnik, E. Feldblum, C. Tamburu, M. Peres, U. Raviv, *Langmuir* **2012**, *28*, 2604–2613; b) O. Szekely, A. Steiner, P. Szekely, E. Amit, R. Asor, C. Tamburu, U. Raviv, *Langmuir* **2011**, *27*, 7419–7438; c) P. Szekely, R. Asor, T. Dvir, O. Szekely, U. Raviv, *J. Phys. Chem. B* **2012**, *116*, 3519–3524; d) P. Szekely, A. Ginsburg, T. Ben-Nun, U. Raviv, *Langmuir* **2010**, *26*, 13110–13129; e) T. Dvir, L. Fink, R. Asor, Y. Schilt, A. Steinar, U. Raviv, *Soft Matter* **2013**, *9*, 10640–10649; f) T. Dvir, L. Fink, Y. Schilt, U. Raviv, *Langmuir* **2014**, *30*, 14725–14733.

[3] J. Als-Nielsen, D. McMorrow, *Elements of Modern X-ray Physics*, 2nd Edition, John Wiley & Sons, Chichester, **2011**.

[4] M. Nadler, A. Steiner, T. Dvir, O. Szekely, P. Szekely, A. Ginsburg, R. Asor, R. Resh, C. Tamburu, M. Peres, U. Raviv, *Soft Matter* **2011**, *7*, 1512–1523.

[5] A. Hammersley, S. Svensson, M. Hanfland, A. Fitch, D. Hausermann, *High Pressure Res.* **1996**, *14*, 235–248.

[6] W. Gander, W. Gautschi, *BIT Numerical Mathematics* **2000**, *40*, 84–101.

[7] G. B. Thomas, R. L. Finney, M. D. Weir, *Calculus and Analytic Geometry*, Vol. 7, Addison-Wesley, Reading, MA, **1988**.

[8] K. E. Atkinson, *An Introduction to Numerical Analysis*, 2nd Edition, John Wiley & Sons, **2008**.

[9] a) S. Kler, R. Asor, C. L. Li, A. Ginsburg, D. Harries, A. Oppenheim, A. Zlotnick, U. Raviv, *J. Am. Chem. Soc.* **2012**, *134*, 8823–8830; b) G. Saper, S. Kler, R. Asor, A. Oppenheim, U. Raviv, D. Harries, *Nucleic Acids Res.* **2013**, *41*, 1569–1580.

[10] a) S. Mukherjee, M. Abd-El-Latif, M. Bronstein, O. Ben-nun-Shaul, S. Kler, A. Oppenheim, *PLoS One* **2007**, *2*, e765; b) S. Mukherjee, S. Kler, A. Oppenheim, A. Zlotnick, *Virology* **2010**, *397*, 199–204.

Received: May 8, 2015
Accepted: July 16, 2015
Published online: November 11, 2015